Preparation and Mechanical Properties of UV‑Assisted Filament Winding Glass Fiber Reinforced Polymer‑Matrix Composite

CHEN Xiaodong[1] , *LI Yong*[2*] , *HUAN Dajun*[1] , *WANG Wuqiang*[1] , *LIU Li*[1]

1. College of Materials Science and Technology, Nanjing University of Aeronautics and Astronautics, Nanjing 211106, P.R. China;

2. National Key Laboratory of Science and Technology on Helicopter Transmission, Nanjing University of Aeronautics and Astronautics, Nanjing 210016, P. R. China

Abstract: This paper studied the preparation and mechanical properties of glass fiber reinforced polymer-matrix composite rings prepared by filament winding assisted by ultraviolet (UV) curing. A ray-tracing method was used to calculate the penetration ability of UV light in the resin casting, and then a typical composite ring with dual‑curing characteristics was prepared by UV-assisted curing. The effects of winding speed and thermal initiator concentration on the distribution of fiber fraction and mechanical properties were studied. Microscopic morphology was used for the observation of the differences in fiber volume fraction. Mechanical properties tests and scanning electron micrographs were performed to investigate the failure and damage mechanisms of the composite ring samples. The ray tracing results indicate that the UV light can pass through a single yarn thickness and the energy transmitted is sufficient to cure the back side quickly. The experimental results show that the mechanical properties of the composite ring prepared in this paper are comparable to those of the heat-cured samples, which is sufficient to meet the requirements of the flywheel.

Key words: glass fiber reinforced polymer (GFRP); ultraviolet (UV) curing; dual-curable resin; mechanical properties; fiber volume fraction

0   Introduction

High-performance continuous fiber-reinforced resin matrix composites are widely used in various fields such as aircraft[1-3], wind turbine rotor blades[4-6] and flywheel rotors[7-9] due to their advantages of high strength to weight and high stiffness to weight ratios. Among them, the composite flywheel rotor is generally produced by a filament winding process[10-12], which is of low cost and high efficiency. The application of rapid curing technics could effectively improve the energy storage performance of flywheel, such as ultraviolet (UV), microwave, and electron beam curing methods[13-15].

The flywheel rotor made of high-strength continuous fiber reinforced composite material can achieve a storage density of 17.6 times that of martensitic steels[16], as claimed by Conteh et al. The energy storage density is proportional to the mass and to the square of its rotational speed[17]. Therefore, the increase in rotational speed can achieve a significant increase in the energy storage density. Refs.[18-20] indicated that when the flywheel rotor rotated at high speed, the radial delamination may occur prior to the fiber breakage in the circumferential direction. The introduction of fiber pre-stress

can alleviate radial delamination damage, while rapid curing resin can effectively maintain the stress on the fiber.

According to the reports of Gutowski et al.[21-25], the fiber stress in filament winding is composed of three parts: the initial fiber tension caused by winding tension, the change of fiber tension caused by fiber movement, and stress relaxation caused by thermal expansion or contraction and chemical changes. Applying of rapid curing resin as a matrix, the viscosity of the resin can be increased rapidly during the winding process, so that the radial displacement of the fiber can be reduced and the initial fiber tension can be retained. The rapid curing resin system comprises thermal curing and radiation curing, wherein the time of thermal curing is as fast as a couple of minutes, while the radiation curing may take only a few seconds. Among radiation curing methods, the UV cationic curing resin has characteristics of rapid initiation, rapid growth (which will increase the viscosity in short time and maintain the winding tension), and difficulty in termination that provides an advantage for post-cure treatment to improve interlayer performance. Refs.[26-27] proposed a layer-wise curing method to overcome the poor penetration performance of UV curing, but the effect is not significant. The maximum tensile strength and shear strength of composite prepared only by UV exposure in Ref.[27] are 902 MPa and 25 MPa, respectively. Tena et al. reported a series research on UV-assisted out of die pultruded composites, the shear strength could reach 50 MPa and the flexural strength was about 833 MPa[28-30]. Endruweit et al.[31-33] addressed that UV light can transmit through voids between the fiber meshes and through the fiber meshes, and dual-curing resin formulations would post cure the resin shadowed by fibers. Compared with thermal curing, UV curing has characteristics of low energy consumption, fast curing speed and environmental friendliness. However, the poor penetrability of UV light restricts its application in composite preparation.

In this paper, the UV penetrability in resin castings was quantitatively analyzed by ray tracing method, a dual-curable resin matrix with two-stage curing characteristics was proposed. A-stage was excited by UV to achieve a rapid and high degree of crosslinking before the prepreg entering the winding mandrel. B-stage was initiated by heating to ensure the bonding strength between the layers. The objective of this paper is to obtain the penetration efficiency of UV light in the sample, and prepare the UV-assisted curing glass fiber reinforced composite material.

1 Modeling

In order to examine the UV exposure dose needed in the pretreatment process quantitatively, a model containing UV intensity distribution on the specimen surface and internal as a function of position was established. Firstly, the UV light source was divided into finite elements. Then a random sampling rule for light-emitting points and orientations was set up. Finally every beam of light was allocated with a certain amount of intensity by

$$E_e = \frac{E_0}{m} \qquad (1)$$

where E_0 is the initial intensity of UV lamp and m the sampling number of light source.

UV intensity distributions would be obtained by tracking the path of each light, and the loss of light passing through the medium was calculated without considering the fluctuations and polarization of light. The parabolic cylinder reflector was also divided into finite elements which were small enough to approach the real surface. Only one time reflection was in consideration during the curing process and assuming that there was no intensity loss when reflected.

1.1 Coordinate of UV lamp

The UV lamp system used in this paper was consisted of a cylinder modulator tube and a parabolic cylinder reflector. Two coordinate systems were used in the simulation. A Cartesian coordinate system was used to describe the position of UV lamp (Fig.1). Fig.1 contains a Cartesian coordinate system (X, Y, Z) and a spherical coordinate system (r, γ, ρ), where P is a random point on the lamp,
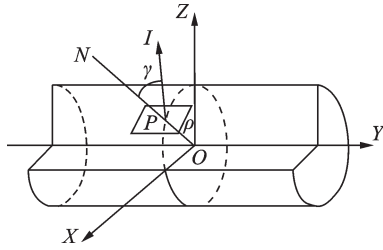
Fig.1   Coordinate system of UV lamp

ρ the azimuth angle, γ the scattering angle of P, and I the normal of the plane tangent to the tube surface and passing through P. The origin of coordinate is the center of the UV lamp, the Y axis is the same line as the central line of the cylinder UV lamp, and the Z axis is perpendicular to the specimen surface. The cylindrical lamp has a radius of r and a length of h. A moving spherical coordinate system, whose origin is determined by the position of emitting point $P(x_1, y_1, z_1)$, was used to trace the light trajectory. In this spherical coordinate system, the scattering angle is $\gamma \in [0, \pi/2]$, and the azimuth angle is $\rho \in [0, 2\pi]$. The direction of the emitting light at this point can be expressed as $\boldsymbol{n} = (n_1, n_2, n_3)$ and determined by the included angle of $\overrightarrow{PN}$ and the normal of the tangent plane through the intersection point of $\overrightarrow{PN}$ and cylindrical surface $\gamma \in [0, \pi/2]$.

1. 2   Sampling of UV lights

The position and direction of UV lights were described based on a pseudo-random number ξ_i, which was uniformly distributed over the range of $[0, 1]$. Combined with geometric constraint equations and random sampling rules, the trajectory of each light can be determined.

The sampling of emitting point P can be derived from

$$\begin{cases} x_1 = r\sin\rho = r\sin(2\pi\xi_1) \\ y_1 = h\xi_2 - \dfrac{h}{2} \\ z_1 = r\cos\rho = r\cos(2\pi\xi_1) \end{cases} \quad (2)$$

where r is the radius of lamp, h the length of the lamp, and ξ_1, ξ_2 are random numbers. (x_1, y_1, z_1) is the coordinate of P. The sampling of emitting direction $\boldsymbol{n} = (n_1, n_2, n_3)$ can be derived from

$$\begin{cases} n_1 = \sin\theta\cos\phi = \sin(\arccos(1 - \xi_4))\cos(2\pi\xi_3) \\ n_2 = \sin\theta\sin\phi = \sin(\arccos(1 - \xi_4))\sin(2\pi\xi_3) \\ n_3 = \cos\theta = 1 - \xi_4 \end{cases} \quad (3)$$

where ξ_3 and ξ_4 are random numbers. A random point $F(x, y, z)$ on the parabolic cylinder reflector can be determined by

$$\begin{cases} x^2 = 2p\left(\dfrac{p}{2} + z\right) \\ y = c \end{cases} \quad (4)$$

where c is a constant $(-a \leqslant c \leqslant a)$, p the focal length of the parabolic cylinder, and a the half length of the parabolic cylinder. The sampling of $F(x_0, y_0, z_0)$ on the parabolic cylinder reflector can be derived from

$$\begin{cases} x_0 = l\cos\pi\xi_5 \\ y_0 = a\cos\pi\xi_6 \\ z_0 = (l^2\cos^2\pi\xi_5 - p^2)/2p \end{cases} \quad (5)$$

where (x_0, y_0, z_0) is the coordinate of F, l the opening width of the parabolic reflector, and ξ_5, ξ_6 are random numbers. The vector of incident light $\boldsymbol{n}_0 = (u_0, v_0, w_0)$ can be described as

$$\begin{cases} u_0 = x_0 - x_1 \\ v_0 = y_0 - y_1 \\ w_0 = z_0 - z_1 \end{cases} \quad (6)$$

The normal of tangent plane through the intersection point of incident light and cylindrical reflector surface can be described as $\boldsymbol{N}$. According to differential geometry[34], the vector of reflected light $\boldsymbol{n} = (n_{11}, n_{22}, n_{33})$ can be described as

$$\boldsymbol{n} = \boldsymbol{n}_0 - 2(\boldsymbol{N} \cdot \boldsymbol{n}_0)\boldsymbol{N} \quad (7)$$

The position of the reflected lights on specimen surface can be described as $P_1(x_2, y_2, z_2)$, that is

$$\begin{cases} x_2 = x_0 + n_{11}(h + z_0) \\ y_2 = y_0 + n_{22}(h + y_0) \\ z_2 = -h \end{cases} \quad (8)$$

2   Experiment

2. 1   Materials and equipment

The Diphenol A epoxy (E51) used as monomer was obtained from Nan Tong Xing Chen Synthetic Material Co., Ltd, and mainly contributed to

the mechanical properties of resin. The Triarylsulfonium hexafluoroantimonate (Chivacure1176) used as photoinitiator was provided by Chitec Technology Co., Ltd. The boron trifluoride-benzylamine complex (BF₃-BZA) used as thermal initiator was purchased from Shanghai Macklin Biochemical Co., Ltd. This thermal initiator used for B-stage curing exists as solid, white powder at room temperature and sensitive to moisture. High-strength glass fiber (HS6)was supplied by Nanjing Fiberglass R&D Institute with a linear density of 800 g/km, virgin fiber tensile strength of 4 800 MPa, modulus of elasticity of 94 GPa and elongation to break of 5.7%. Acetone was used as solvent to dissolve BF₃-BZA and regulate the viscosity of the resin to better impregnate the fibers, obtained from Shanghai Aladdin Biochemical Technology Co., Ltd. The radiation intensity received by the prepreg was measured using an intensity meter (Sentry Optronics Co., Ltd of Taiwan) which possessed a spectral region of 280—400 nm with a measurement range of 0—40 mW/cm² and a minimum resolution of 0.01 mW/cm².

2. 2   Preparation of reactive resin

In order to better dissolve the photoinitiator, the epoxy resin was heated to 60 ℃ in a magnetically stirred oil bath to reduce its viscosity while avoiding water absorption and then added 5% (in weight) photoinitiator dropwise. After that, the mixture was stirred for 30 min and cooled to room temperature. The thermal initiator dissolved in the acetone solution was then added to the mixture, followed by magnetic stirring for 15 min to uniformly mix. The resin matrix for studying the influence of thermal initiator was prepared in the following ratios：E51∶Chivacure 1176∶Acetone was 100∶5∶8, and the thermal initiator content was used in five different ratios, 0%, 0.5%, 1.5%, 2.5%, and 3.5%, respectively, while the resin matrix for studying the influence of winding speed was prepared in the following ratios：E51∶Chivacure 1176∶BF₃-BZA∶Acetone was 100∶5∶1.5∶8.

2. 3   Fabrication of composite ring (A-stage curing)

The twistless glass fibers from the torque motor was dipped in the resin tank, and the resin content in the prepreg was controlled by adjusting the temperature of the solution and the wrap angle of the fiber on the squeezing rollers.

The preparation of naval ordnance laboratory (NOL) ring referred to American standard ASTM D2291, and the winding tension was maintained at 20 N. The dipped fibers first passed through the UV irradiation zone, and then through a tension detector before entering the winding mold. The two sets of rollers (Fig.2) before and after the UV irradiation area ensured that each fiber passed through the same area. And then, the fiber tension was adjusted to be stabilized at 20 N±2 N by the voltage value of the torque motor according to the feedback information on the tension detector. Finally, the prepreg yarn was guided by the guide mouth to prepare the NOL ring.
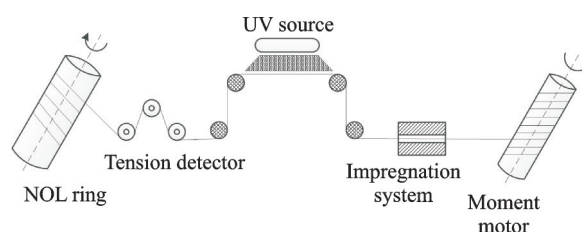
Fig.2   NOL ring fabrication scheme

2. 4   Post-curing of composite ring (B-stage curing)

The prepreg was also seriously subjected to the thermal effects when exposed to the UV mercury lamp. In order to prevent the photoinitiator and the thermal initiator from being simultaneously triggered, BF₃-BZA was chosen as the thermosetting agent. From the DSC curves of the dynamic heating process in Fig.2, it can be determined that the UV reactive resin matrix mixed with BF₃-BZA has an initial curing temperature of 115 ℃ and final curing temperature of 180 ℃. Therefore, after the winding, the NOL ring can be post-treated with a final temperature (180 ℃) and holding time (30 min) to ensure complete curing.

3   Characterizations

3. 1   UV absorption coefficient measurement

In order to eliminate the measurement error caused by the height of UV-meter itself, a UV lamp system was mounted on a mechanical arm to measure the UV light intensity after a relative displacement in the Z direction. During the curing process, the absorption coefficient of the resin with photoinitiator would increase due to the shrink of the volume as presented by Lam et al[35]. Thus, the UV intensity meter would fix on the under glass plate to record the UV intensity at intervals (Fig.3).
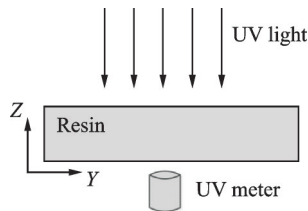
Fig.3   Configuration for measurement of the transmitting radiation and curing mould

3. 2   Test of fiber volume fraction

The distribution of fiber volume fraction in typical samples varies significantly with the winding speed and the curing agent content. It can be seen from the metallographic picture in Fig.4 that there is a significant interfacial resin-rich zone between the layers, and the fiber accumulation in the layer is relatively tight.

In this article, the volume content of fiber and volume content of resin-rich area were calculated by means of the metallographic photographs using ImageJ software. From the metallographic photographs of the cross-section in Fig.4, it can be seen that under the 20 N winding tension, fibers are closely packed with rarely voids, and each fiber is uniformly surrounded with resin. Therefore, it is possible to obtain a more accurate fiber volume fraction using microscopic techniques. In order to reduce errors caused by fiber incompleteness in the metallographic picture, ImageJ software was used in this paper to obtain the average diameter of the fibers, and then the fiber volume content was calculated by

$$\alpha_{vc}^{f} = \frac{n \times d_0}{S} \tag{9}$$

where α_{vc}^{f} is the volume content of fiber, n the fiber numbers of interested region, d_0 the average diameter of fibers, and S the total area of interested region.
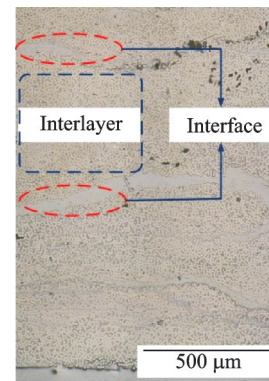
Fig.4   Fiber distribution of cross-section

3. 3   Mechanical properties of composite ring

The tensile strength and shear strength test were performed on the MTS test machine with reference to the American standard ASTM D 2290 and ASTM D 2344, respectively. The tensile strength can be determined with the help of Eq.(10), while the shear strength was obtained according to Eq.(11), as shown in Fig.5.

$$\sigma = \frac{P_m}{2 \times b \times d} \tag{10}$$

where σ is the apparent yield or ultimate tensile stress of the specimen (MPa), P_m the maximum or breaking load (N), b the average width of the specimen (mm), and d the average thickness of the specimen (mm).

$$\tau = 0.75 \times \frac{P_m}{b \times d} \tag{11}$$

where τ is interlaminar shear strength of the speci-

(a) Tensile test   (b) Shear test
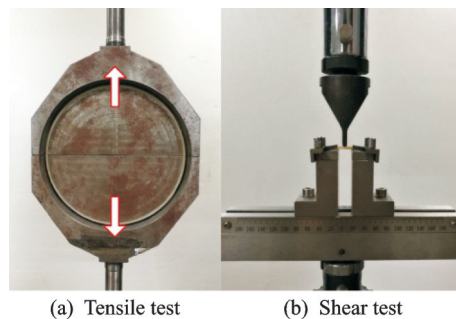
Fig.5   Test of mechanical properties

men, MPa.

4   Results and Discussion

4.1   Results of UV absorption coefficient measurement

The UV light would pass through three different media: air, glass plate and resin before reaching the UV-meter. UV light distribution after transmitting through these media would maintain a slight difference (less than 5% in the range of 10 cm centered on the x-axis origin), if the surrounding environment remains stable. However, after transmitting through resin with photoinitiator the UV light distribution would change a lot as presented by Lam et al[35]. According to the Beer-Lambert law

$$E_t = E_0 \exp(-\mu H) \qquad (12)$$

where E_0 is the initial intensity, μ the absorption coefficient and H the distance. After passing through the medium, the UV light intensity received by UV-meter can be obtained by

$$E(x_t, y_t, z_t) = E(x_0, y_0, z_0)\exp\left(-\sum_{i=1}^{n} \mu_i H_i\right) \quad (13)$$

where μ_i and H_i are the absorption coefficients and thicknesses of the air, the upper glass plate, the resin and the lower glass plate, respectively. The measured values for different media with a relative displacement and corresponding absorptions for μ_i, determined according to Eq.(13), are listed in Table 1. Distribution of absorption coefficient is shown in Fig.6.

Table 1   UV light intensity with relative displacements and the absorption coefficient μ_i as derived from Eq.(13)

Material name	UV light intensity/(mw·cm^{-2})	Relative displacement/cm	Absorption coefficient/cm^{-1}
Air$_{z_0}$	22.68	5.00	0.08(μ_1)
Air$_{z_1}$	15.19		
Glass plate$_{z_0}$	28.04	2.40	0.59($\mu_2 = \mu_4$)
Glass plate$_{z_1}$	13.86		
Resin$_{z_0}$	28.04	0.20	1.18(μ_3)
Resin$_{z_1}$	22.13		

Fig.6   Schematic diagram of distribution of absorption coefficient

In addition, the UV ht distribution after passing through resin with photoinitiator was measured as shown in Fig.7.

With the increasing of exposure time, the received UV light intensity decreased to nearly a platform value after a quasi-linear drop in the first 20 s as shown in Line 1. As mentioned previously, the reaction resin consists of monomer and photoinitiator. The photoinitiator has a strong selective absorption of UV light, while the monomer is almost transparent to UV light. The transmittance of the resin with
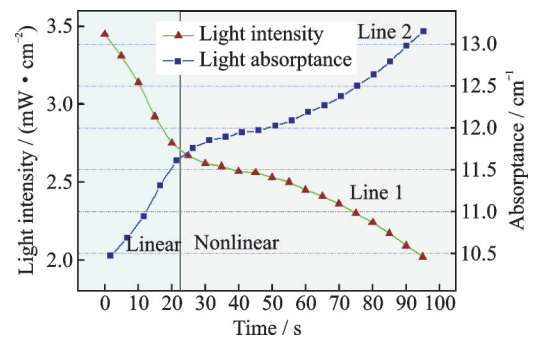
Fig.7   Light intensity and light absorption value change over time for resin with photoinitiator

the UV exposure process seems to increase gradually with the gradual depletion of the photoinitiator. However the resulting reactive groups will rapidly initiate polymerization of the monomers with continuous consumption of the photoinitiator, which will lead to a rise in resin viscosity and a significant change in the absorption coefficient. The absorption of resin with photoinitiator was obtained as shown in Line 2 according to Eq.(13). It was found that with-

in a point the refractive index increased linearly with conversion to gel point[35]. Based on the optical theory of light, if the refractive index of a medium is defined as a complex number in Eq.(14), it can be seen from Eq.(15) that the imaginary part of the refractive index of the medium reflects the attenuation due to the absorption of light[36]. Combined with Fresnel's law, the linear variation of the intensity distribution of the first 20 s was obtained by linear fitting in Eq.(16).

$$\widetilde{n} = n(1 + \mathrm{i}k) \tag{14}$$

where n and k are both real numbers.

$$E_t = E_0 \exp(-4\pi H n k / \lambda_0) \tag{15}$$

where λ_0 is the wavelength in vacuum.

$$\mu = 0.058 \times t + 10.425 \tag{16}$$

where t is the curing time and μ the coefficient of absorptance.

4.2   Modeling of light distribution in resin

For the light transmission in resin with photo-initiator, the absorption coefficient can simply be taken as 10.425 cm^{-1} for the initial absorption and 11.585 cm^{-1} for the cured absorption according to Eq.(16) in the first 20 s. During the initial curing process, assuming that the polymerization occurred instantaneously[37], the absorption coefficient would be updated with the curing process.

Since the location and orientation of UV light received on the sample was obtained, the distribution of UV intensity on the upper surface can be quantified (Fig.8).

It can be seen from Fig.8 that there was a quasi-uniform area centered on zero point of position axis with a higher light intensity. The intensity distribution curve of light intensity at different depths was shown in Fig.9. The quasi-uniform area was of 20 cm long in the y direction and of 15 cm wide in the x direction. It can be seen that the middle area of the light intensity distribution in x-axis plane (Fig.9 (a)) gradually stabilized with the increased UV penetration depth.

When the thickness increased to 0.08 cm, the penetrated UV intensity was almost below the threshold value that was determined by Ma's experi-

(a) Depth of 0 cm   (b) Depth of 0.02 cm

(c) Depth of 0.04 cm   (d) Depth of 0.06 cm

(e) Depth of 0.08 cm   (f) Depth of 0.10 cm
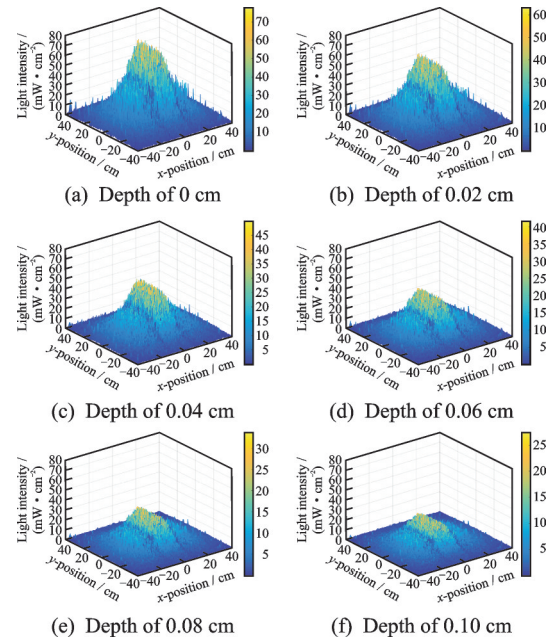
Fig.8   Three-dimensional morphology picture of light intensity distribution in the resin thickness direction

(a) Projection of light intensity in x-axis plane

(b) Projection of light intensity in y-axis plane
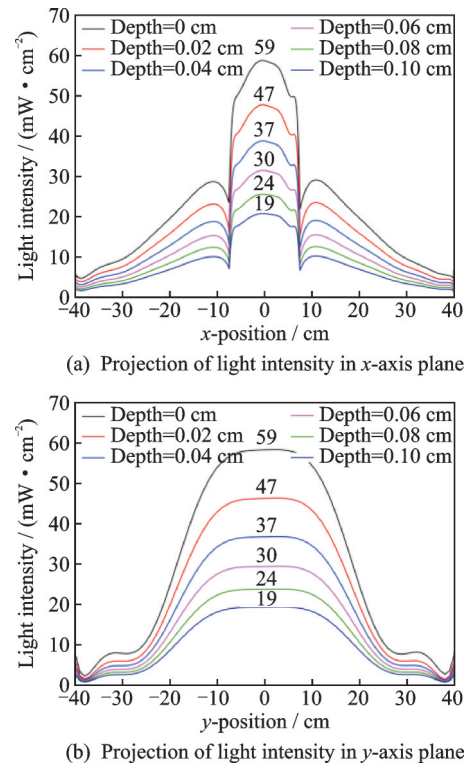
Fig.9   Light intensity distribution curve of resin in the thickness direction

ment (28.79 mw/cm^2)[38](Fig.9(b)). It was reported that when ultraviolet light penetrated through one layer of glass fiber fabric, the remaining energy of UV light remains more than 62%[31]. The penetration efficiency of ultraviolet light in unidirectional glass fiber is larger than that of fabric. Therefore,

the intensity of UV light after it penetrates 0.02 cm thick prepreg （47 mW/cm² × 62% > 28.79 mW/cm²） when the fiber is present can still reach the curing threshold. Once the UV energy exceeds the cure threshold, the photosensitive resin polymerizes and crosslinks rapidly, as shown in Fig.7.

4.3 Effect on fiber volume fraction

The fiber volume fraction in the component is largely determined by the resin content of the prepreg. In this paper, the resin content in the prepreg was controlled in the range of 30% ± 5%, the fiber volume fraction depends mainly on the percolation of the resin in the yarn. If the viscosity of the resin in the prepreg is low, the interlaminar resin will penetrate the surface of the part or accumulate in the gap of the yarn under the action of the fiber pressure, resulting in a high fiber volume fraction. If the viscosity of the prepreg is high, the resin flow effect is not significant, resulting in a low fiber volume fraction.

It can be seen from Fig.10 that the fiber volume fraction first increases to 60.3% and then de-

(a) Influence of winding speed

(b) Influence of thermal agent concentration

Fig.10   Influence of winding speed and percentage content of cure agent on fiber volume fraction

creases as the winding speed increases from 50 mm/s to 150 mm/s. The volume fraction of the resin-rich zone first drops to 0.6% and then rises, the minimum fiber volume fraction and the largest volume content of resin-rich zone all appear at a winding speed of 50 mm/s, which are 51.9% and 8.2%, respectively. At the same time, with the increase of the percentage content of BF_3-BZA, the fiber volume fraction also increases first and then decreases, and the volume fraction of the resin-rich zone decreases first and then increases. When the content of the thermal curing agent is 1.5%, the fiber volume fraction reaches the maximum percentage at 60.3%, on the other hand the volume fraction of resin-rich zone is the minimum percentage at 4.0%.

Prior to thermal curing, the viscosity of the resin matrix increased due to the passage of UV lamp. The degree of crosslinking depended on the intensity of ultraviolet radiation on the surface of the prepreg, which was determined by the winding speed because the power of the UV lamp and the distance between the lamp and the fiber yarn were fixed. Assuming that the ultraviolet irradiation intensity did not change with time, the ultraviolet light intensity received per unit distance of the prepreg can be calculated from Eq.(17).

$$E = P \times \frac{L_0}{v \times b \times d} \tag{17}$$

where P is the light intensity of the surface of the prepreg yarn （mW）, L_0 the effective irradiation length of the ultraviolet mercury lamp （mm）, v the winding speed of the prepreg yarn （mm/s）, b the width of prepreg, and d the unit length of prepreg.

4.4 Effect of winding speed on mechanical properties

The role of the matrix material in the composite material is mainly to bond the dispersed fibers and transfer the load to fibers through the interface between fiber and resin during loading so as to achieve the purpose that the reinforcement fibers can evenly bear the external load. If the fiber volume content of the composite material is distributed in the thickness direction unevenly, especially in the large tension winding samples, there will be a grad-

ual failure in the loading process.
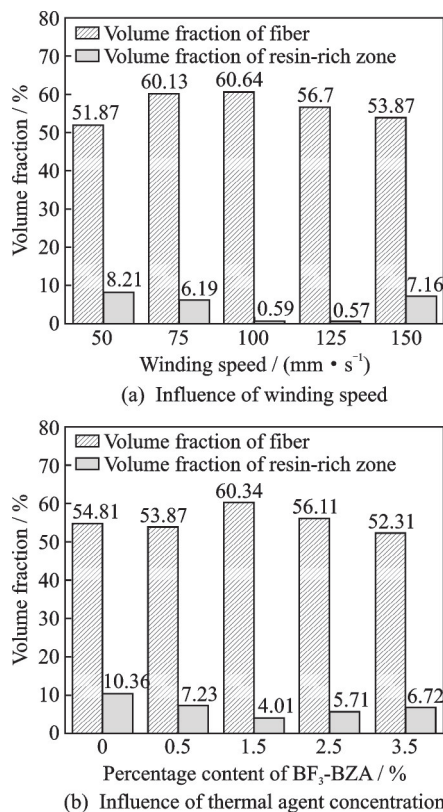
As the winding speed decreased, the UV irradiation intensity increased correspondingly, and the tensile strength and interlaminar shear strength (ILSS) of composites shared a consistent trend, which increased at first and then decreased (Fig.11). When the winding speed reached 75 mm/s, the highest average tensile strength was 1 582.32 MPa and the maximum shear strength was 35.37 MPa, which was 50.3% and 60.0% higher than the sample without UV light, respectively. However, when the winding speed changed from infinity (no UV exposure) to 150 mm/s, which means a slight increase of UV intensity, the tensile strength was increased by 30.7%, and the shear strength was increased by 22.3%. It can be seen that proper increase of illumination can significantly improve the mechanical properties of the composite. The reason may be that the heat curing dose of 1.5% (in weight) is too small, and in the absence of the A-stage curing, the degree of crosslinking of the resin during the B-stage is insufficient, so the interlaminar shear strength is low, and the interlayer resin cannot sufficiently transfer the load of the fiber during the tensile test, therefore a small amount of UV exposure can significantly improve the mechanical properties of the sample. When the speed was less than 75 mm/s, the interlaminar shear strength and tensile strength began to decrease, which may be caused by the high degree of crosslinking in A-stage curing. The viscosity of prepreg became high due to the crosslinking in A-stage curing, and resin-rich regions were then formed between the layers, which cannot be eliminated during the B-stage curing, resulting in the presence of resin-rich zone in the sample as shown in Fig.4.

From the force-displacement curve of the NOL ring tensile test (Fig.12), it is obvious that the sample prepared by winding speed of 75 mm/s shows a slight load reduction before the failure, and the load change value is relatively small, while the remaining samples show more than a few different levels of load reduction before failure. There are two typical failure modes as shown in Fig.13, namely fiber cracking and delamination. A lower fiber volume

(a) Tensile strength

(b) Shear strength
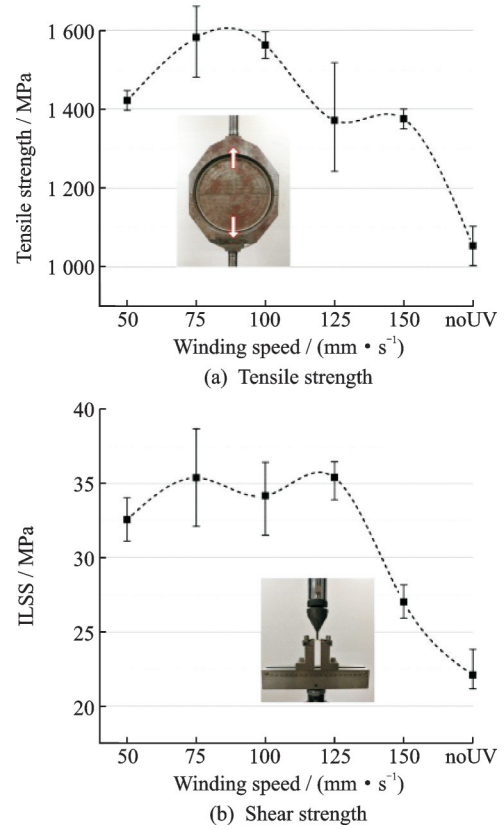
Fig.11   Mechanical properties of different winding speed

(a) Different winding speed

(b) Different thermal initiator content
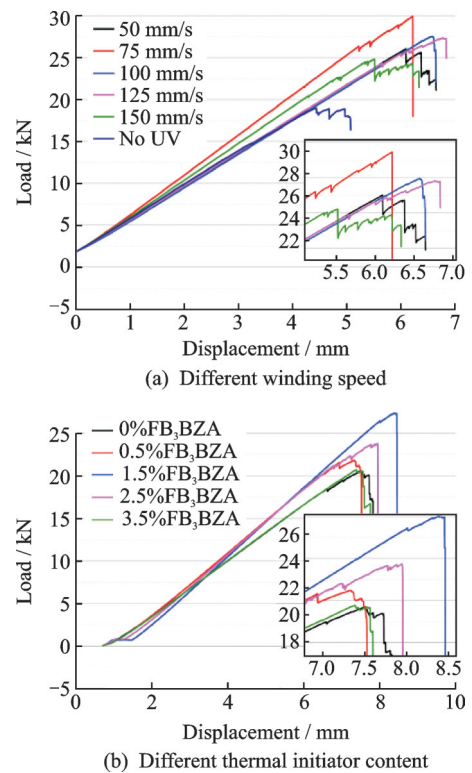
Fig.12   Force-displacement curve of NOL ring tensile test

fraction tends to exhibit a uniform fracture pattern, and a higher fiber volume fraction is prone to delamination and lateral tear fracture.

(a) Main feature of fiber cracking

(b) Main feature of debonding
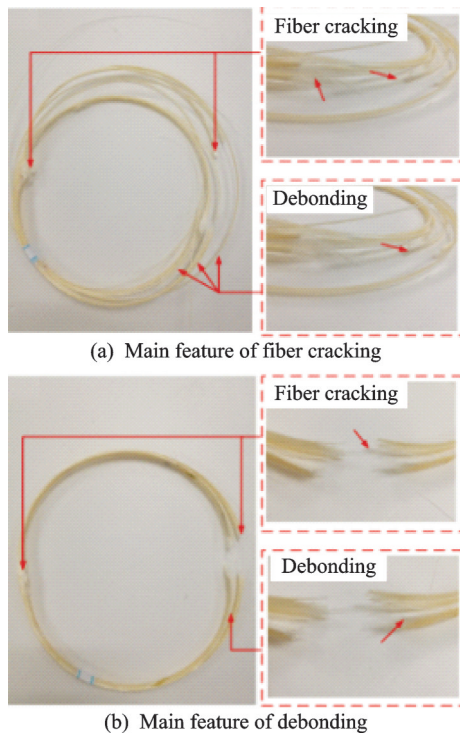
Fig.13   Different failure mode of tensile samples

It can be seen from the scanning electron microscopy (SEM) fracture photograph (Fig.14) of the typical interlaminar shear specimen that the fracture surface has obvious cusps and fiber imprints. When the winding speed increases, the cusps steps become shallower following deeper cusps on the surface at winding speed of 75 mm/s (Fig. 14(a)). Here the cusp tilt direction on the fiber dominated fracture surfaces referred to the opposite direction to

(a) 75 mm/s

(b) 150 mm/s

(c) no UV
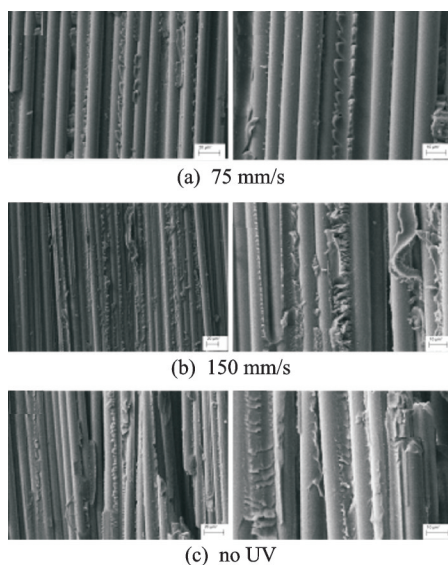
Fig.14   SEM images of ILSS samples at different winding
speed

the crack growth direction[39]. At winding speed of 150 mm/s, a ribbon was observed in Fig. 14(b). The cusps of the fracture surface of shear sample without UV exposure almost converges to a plane (Fig.14(c)), and the crack propagation path is significantly shortened, resulting in low shear strength.

4. 5   Effect of thermal curing agent on mechanical properties

The tensile strength and interlaminar shear strength of the composite material also increase in the first and then decrease with the percentage content of thermal initiator growing (Fig.15). The interlaminar shear strength reaches a maximum value of 37.04 MPa when the percentage of thermal initiator is 2.5%, which is 81.9% higher than the sample without thermal curing, meanwhile when the percentage of the thermal initiator is 1.5%, the NOL ring tensile properties of the composite reaches a maximum value of 1371.59 MPa, which is 23.8% higher than the sample of no thermal initiator. Therefore, the amount of thermal curing had a significant effect on the mechanical properties of the NOL ring of the composite material. The best per-

(a)   Tensile strength

(b)   Shear strength
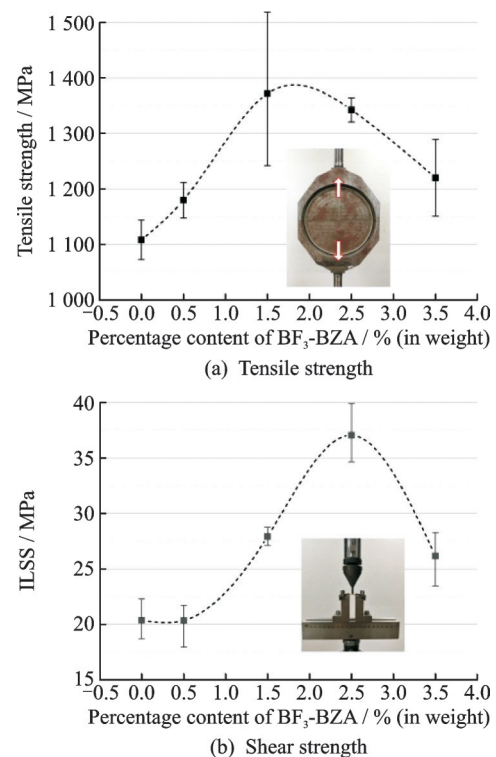
Fig.15   Mechanical properties of different thermal initiator
content

formance of mechanical properties is achieved between 1.5％ and 2.5％ of the thermal initiator. When the percentage of thermal initiator exceeds 1.5％, the crosslinking density of B-stage curing of the resin increases, which might lead to a decrease of resin toughness and an increase of resin brittleness. This may be the reason why the optimum tensile strength and the best shear strength do not appear in the same curing agent concentration. At the same time, when the thermal initiator content changed from 0 to 0.5％, the tensile strength was increased by 6.4％, while the shear strength remained almost the same. Thus, the excessive or insufficient heat curing agent content cannot obtain good mechanical properties.

There is no obvious cusp can be observed in the scanning photomicrograph without thermal initiator in Fig.16(a). It may be caused by the insufficient cure in B-stage. As the thermal initiator percentage content increased from 2.5％ to 3.5％, the size of cusps become smaller while the number has increased. This may be due to the increased brittleness of the resin. The tensile strength and shear strength obtained by the optimum winding speed and the optimum heat curing agent content reached 70％ and 71％, respectively, of the properties of the heat-cured sample.

(a) 0%

(b) 2.5%

(c) 3.5%
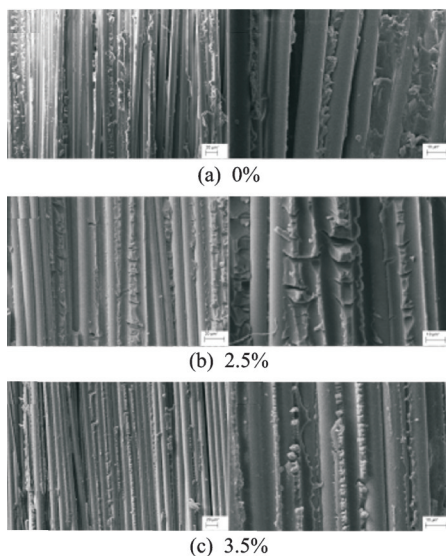
Fig.16   SEM images of ILSS samples at different thermal initiator concentration

5   Conclusions

In the preparation of the composite flywheel rotor, the pre-stress level is difficult to accurately control due to the radial displacement of the fiber. The UV-assisted rapid curing resin system with two-stage curing characteristics can alleviate the fiber displacement along radial direction while ensuring the mechanical properties of the component. In this paper, an UV light initiated dual-curable resin matrix was used to study the mechanical properties of composite samples with constant winding tension. The effect of different winding speeds and different thermal initiator concentrations on performance was investigated. Moreover, microscopic observations were used to understand the failure mechanisms. The following conclusions are obtained:

(1) A model of UV light was established and the distribution of light intensity on the surface of the specimen and inside the specimen was quantified. When the thickness of the unidirectional prepreg is less than 0.2 mm, the ultraviolet light transmitted through the prepreg is sufficient to cure the resin quickly.

(2) A resin-rich zone was observed in most of the samples herein, when the winding speed was the 75 mm/s, the thermal initiator content was zero, and the volume fraction of the resin-rich zone was the largest, respectively, but as the winding speed increased and the thermal initiator increased, the volume fraction of the resin-rich zone eventually began to increase.

(3) When the winding speed changed from infinity (no UV exposure) to 75 mm/s, the tensile strength was increased by 50.3％, and the shear strength was increased by 60.0％, meanwhile when the thermal initiator content changed from 0 to 1.5％, the tensile strength was increased by 23.8％, and when the thermal initiator content changed from 0 to 2.5％, the shear strength was increased by 81.9％.

(4) A small amount of light intensity can significantly improve the mechanical properties of the component, while the effect of a small amount of

thermal initiator was not significantly increased, but excessive UV or thermal initiators would lead to performance degradation.

(5) The composite material prepared by the UV-assisted dual-curable resin in this article had excellent mechanical properties, and reliable performance data. It can be used as a resin matrix for large tension winding experiment, and further research should be conducted in the tension retention rate.

References

[1] BOGETTI T A, Jr GILLESPIE J W. Two-dimensional cure simulation of thick thermosetting composites[J]. Journal of Composite Materials, 1991, 25(3): 239-273.

[2] ZHANG Lin, TIAN Wei, LI Dawei, et al. Design of drilling and riveting multi-functional end effector for cfrp and aluminum components in robotic aircraft assembly[J]. Transactions of Nanjing University of Aeronautics & Astronautics, 2018, 35(3): 529-538.

[3] LIU Rongmei, XIAO Jun, LIANG Dakai, et al. Performance improvement method of CFRP with embedded optical fiber[J]. Transactions of Nanjing University of Aeronautics & Astronautics, 2015, 32(3): 261-267.

[4] XU Jiazhong, YU Ying, QIAO Ming, et al. Numerical simulation research on curing process of composite overwrap considering a die model[J]. Journal of Reinforced Plastics and Composites, 2013, 32(19): 1393-1405.

[5] QIU Jinhao, TAO Chongcong, JI Hongli, et al. Damage detection and material property reconstruction of composite laminates using laser ultrasonic technique[J]. Transactions of Nanjing University of Aeronautics & Astronautics, 2019, 36(1): 3-19.

[6] ZANGENBERG J, BR NDSTED P, KOEFOED M. Design of a fibrous composite preform for wind turbine rotor blades[J]. Materials & Design (1980—2015), 2014, 56: 635-641.

[7] MOUSAVI G S M, FARAJI F, MAJAZI A, et al. A comprehensive review of flywheel energy storage system technology[J]. Renewable and Sustainable Energy Reviews, 2017, 67: 477-490.

[8] KALE V, SECANELL M. A comparative study between optimal metal and composite rotors for flywheel energy storage systems[J]. Energy Reports, 2018, 4: 576-585.

[9] HIROSHIMA N, HATTA H, KOYAMA M, et al. Optimization of flywheel rotor made of three-dimensional composites[J]. Composite Structures, 2015, 131: 304-311.

[10] HA S K, KIM S J, NASIR S U, et al. Design optimization and fabrication of a hybrid composite flywheel rotor[J]. Composite Structures, 2012, 94(11): 3290-3299.

[11] KIM S J, HAYAT K, NASIR S U, et al. Design and fabrication of hybrid composite hubs for a multi-rim flywheel energy storage system[J]. Composite Structures, 2014, 107: 19-29.

[12] SAYEM UDDIN M, MOROZOV E V, SHANKAR K. The effect of filament winding mosaic pattern on the stress state of filament wound composite flywheel disk[J]. Composite Structures, 2014, 107: 260-275.

[13] MGBEMENA C O, LI D, LIN M F, et al. Accelerated microwave curing of fibre-reinforced thermoset polymer composites for structural applications: A review of scientific challenges[J]. Composites Part A: Applied Science and Manufacturing, 2018, 115: 88-103.

[14] BEREJKA A J, EBERLE C. Electron beam curing of composites in North America[J]. Radiation Physics and Chemistry, 2002, 63(3): 551-556.

[15] COMPSTON P, SCHIEMER J, CVETANOVSKA A. Mechanical properties and styrene emission levels of a UV-cured glass-fibre/vinylester composite[J]. Composite Structures, 2008, 86(1): 22-26.

[16] XU J Z, QIAO M, YOU B, et al. Research on heated-mandrel winding process for resin-matrix composite shells[J]. Journal of Reinforced Plastics and Composites, 2012, 31(9): 605-620.

[17] BOLUND B, BERNHOFF H, LEIJON M. Flywheel energy and power storage systems[J]. Renewable and Sustainable Energy Reviews, 2007, 11(2): 235-258.

[18] WANG Yong, DAI Xingjian, WEI Kunpeng, et al. Progressive failure behavior of composite flywheels stacked from annular plain profiling woven fabric for energy storage[J]. Composite Structures, 2018, 194: 377-387.

[19] TZENG J, EMERSON R, MOY P. Composite flywheels for energy storage[J]. Composites Science and Technology, 2006, 66(14): 2520-2527.

[20] OKOU R, SEBITOSI A B, PILLAY P. Flywheel rotor manufacture for rural energy storage in sub-Saharan Africa[J]. Energy, 2011, 36(10): 6138-6145.

[21] ZHOU Jing, LI Yingguang, LI Nanya, et al. Interfacial shear strength of microwave processed carbon fiber/epoxy composites characterized by an improved fi-

ber-bundle pull-out test[J]. Composites Science and Technology, 2016, 133: 173-183.

[22] LEE S Y, SPRINGER G S. Filament winding cylinders: I—Process model[J]. Journal of Composite Materials, 1990, 24(12): 1299-1343.

[23] CALIUS E P, LEE S Y, SPRINGER G S. Filament winding cylinders: II—Validation of the process model[J]. Journal of Composite Materials, 1990, 24 (12): 1299-1343.

[24] GUTOWSKI T G. Advanced composites manufacturing[M]. New York: John Wiley & Sons, Inc, 1997.

[25] CHEN Zhi, ZENG Jianjiang, TONG Mingbo. Effect of tension field on joint strength of CFRP beam[J]. Journal of Nanjing University of Aeronatuics & Astronautics, 2018, 50(1): 36-44. (in Chinese)

[26] ZHANG Xiaohui, DUAN Yugang, ZHAO Xinming, et al. UV stepwise cured fabrication of glass fiber/acrylate composites: Effects of exposure dose on curing uniformity and interlaminar shear strength[J]. Journal of Composite Materials, 2016, 50(10): 1395-1401.

[27] DUAN Yugang. Fabrication and mechanical properties of UV-curable glass fiber-reinforced polymer-matrix composite[J]. Journal of Composite Materials, 2011, 45(5): 565-572.

[28] CAMINERO M A, CHAC N J M, GARC A-MORENO I, et al. Interlaminar bonding performance of 3D printed continuous fibre reinforced thermoplastic composites using fused deposition modelling[J]. Polymer Testing, 2018, 68: 415-423.

[29] DELL'ANNA R, LIONETTO F, MONTAGNA F, et al. Lay-up and consolidation of a composite pipe by in situ ultrasonic welding of a thermoplastic matrix composite tape[J]. Materials, 2018, 11(5): 786-797.

[30] BOON Y D, JOSHI S C, ONG L S. Interfacial bonding between CFRP and mechanically-treated aluminum liner surfaces for risers[J]. Composite Structures, 2018, 188: 374-386.

[31] ENDRUWEIT A, RUIJTER W, JOHNSON M S, et al. Transmission of ultraviolet light through reinforcement fabrics and its effect on ultraviolet curing of composite laminates[J]. Polymer Composites, 2008, 29(7): 818-829.

[32] ENDRUWEIT A, JOHNSON M, LONG A. Curing of composite components by ultraviolet radiation: A review[J]. Polymer Composites, 2006, 27 (2): 119-128.

[33] ZHAO Liyang, MANTELL S C, COHEN D, et al. Finite element modeling of the filament winding process[J]. Composite Structures, 2001, 52 (3):

499-510.

[34] GUO H. Differential geometry[M]. New York: MC-GRAW-HILL, 1963.

[35] LAM K Y, AFROMOWITZ M A. Fiber-optic epoxy composite cure sensor. I—Dependence of refractive index of an autocatalytic reaction epoxy system at 850 nm on temperature and extent of cure[J]. Applied Optics, 1995, 34(25): 5635-5638.

[36] BORN M, WOLF E. Principles of optics: Electromagnetic theory of propagation, interference and diffraction of light[M]. New York: Elsevier, 2013.

[37] ADANUR S, ARUMUGHAM Y. Characteristics of ultraviolet cured glass-epoxy composites Part 2: Results and discussion[J]. Journal of Industrial Textiles, 2002, 32(2): 107-118.

[38] MA Desheng, WANG Xiang, WU Changchang, et al. Theoretical analysis and experimental research of solidification shapes for stereo photo lithography[J]. China Mechanical Engineering, 2004 (18): 54-57. (in Chinese)

[39] VASHISTH A, ASHRAF C, ZHANG W, et al. Accelerated ReaxFF simulations for describing the reactive cross-linking of polymers[J]. The Journal of Physical Chemistry A, 2018, 122(32): 6633-6642.

Authors   Mr. **CHEN Xiaodong** received B. S. degree in Materials Processing Engineering from Nanjing University of Aeronautics and Astronautics in 2014. From 2014 to present, he has been with College of Materials Science and Technology, Nanjing University of Aeronautics and Astronautics (NUAA), where he is currently a Ph. D. candidate. His research is focused on preparation and design of composite flywheel rotor.

Prof. **LI Yong** received the B. S. and Ph. D. degrees in Materials Processing Engineering from NUAA, in 1993 and

紫外辅助缠绕玻璃纤维增强树脂基复合材料的制备和力学性能研究

陈晓东[1]，李　勇[2]，还大军[1]，王武强[1]，刘　丽[1]

（1.南京航空航天大学材料科学与技术学院，南京 211106，中国；

2.南京航空航天大学直升机传动技术重点实验室，南京 210016，中国）

摘要：本文研究了紫外辅助固化玻璃纤维增强复合材料缠绕成型环形构件的制备过程和力学性能。基于光线追踪法量化了树脂浇注体中的紫外穿透能力，并制备了紫外辅助固化的光—热双重固化典型样件，研究了缠绕速度和热固化引发剂的浓度对缠绕制件的纤维体积分数和力学性能的影响。纤维体积分数和构件的失效分析分别采用图像法、力学性能测试和扫描电镜测试。光线追踪结果表明：紫外光能够穿透一层纤维束的厚度且背光面透过的紫外能量足以快速引发固化；试验结果表明：本文制备的紫外辅助固化复合材料环形样件与热固化试件相比均能满足飞轮转子对性能的要求。

关键词：玻璃纤维增强复合材料；紫外固化；双重固化树脂；力学性能；纤维体积分数